Atomic Insights into Robust Pt-PdO Interfacial Sites Boosted Hydrogen Generation

Wenyao Chen,[a,#] Weizhong Zheng,[a,#] Junbo Cao,[a] Wenzhao Fu,[a] Gang Qian,[a] De Chen,[b] Xinggui Zhou,[a] Xuezhi Duan[a,*]

[a]*State Key Laboratory of Chemical Engineering, East China University of Science and Technology, Shanghai 200237, China*

[b]*Department of Chemical Engineering, Norwegian University of Science and Technology, N-7491 Trondheim, Norway*

[#]These authors contributed equally to this study.

[*]To whom correspondence should be addressed. Tel.: +86-21-64250937; E-mail: xzduan@ecust.edu.cn.

ABSTRACT: Suppression of catalyst deactivation without compromising activity has been a long-standing yet elusive goal in heterogeneous catalysis. Herein, we report a remarkable achievement of both hydrogen generation activity and durability by atomically engineering Pt-PdO interfacial sites. A combination of kinetics (isotopic) analyses, multiple characterization techniques, molecular dynamics and density functional theory calculations was employed to reveal the evolution of Pt-Pd atomic structure that Pd segregates to the outer surface of Pt nanoparticles followed by partial oxidation, resulting in the structure of a Pt-rich core and a PdO/Pd-rich shell. The strong capability of PdO to activate H_2O compensates for its adverse effects on Pt electronic properties and creates the Pt and PdO interfacial sites for ammonia borane and H_2O activation, respectively. Moreover, due to the strong electron repulsion and steric hindrance effects, these surface PdO sites strongly inhibit the adsorption of $B(OH)_4^-$, thus protecting Pt active sites from poisoning. As a result, such unique atomic structure with a Pt/Pd ratio of 1:1 is found to be the most promising catalyst at the apex of the volcano curve. The strategy developed here unambiguously clarifies the activity and durability attributes of Pt-PdO interfacial sites for this reaction and sheds light on the design of new type of highly active yet stable metal catalysts.

Keywords: Pt-PdO interfacial sites; Atomic insights; Hydrogen generation; Activity and durability; Volcano curve.

1. Introduction

Supported metal catalysts are widely used in industrial chemistry due to their long-term survival, robust recyclability and ease of handling.[1] In pursuit of a high yield for targeted chemicals, the development of newly efficient metal catalysts has attracted tremendous attention from chemists in past decades.[2] Currently, catalyst engineering is undergoing a transition from using the pure trial-and-error approach that necessitates immense screening efforts, to semi-rational design based on a combination of kinetics modeling, isotope labeling, advanced characterizations, computational chemistry and judicious interpretation of the results obtained by these techniques that provide an unprecedented opportunity to design and manipulate metal catalysts with high mass-specific reactivity.[3]

Hydrogen has emerged as a clean energy carrier for future carbon-free energy economy,[4] and the hydrolytic dehydrogenation of ammonia borane (NH_3BH_3, AB) offers a promising and attractive approach for hydrogen production due to the low molecular mass (30.8 $g \cdot mol^{-1}$) and high hydrogen capacity (19.6 wt%) of AB.[5] Although Pt-based catalysts demonstrate much higher catalytic activity compared to other metal catalysts, the prohibitive cost and limited abundance of Pt hinder their widespread adoption.[6] Hence, tremendous efforts have been devoted to the preparation of highly efficient catalysts with low Pt usage via tailoring of the Pt particle composition and size,[7] engineering of the catalyst support properties,[8] alloying with other metals,[9] varying catalyst preparation methods,[10] and adding structural and/or electronic promoters.[11] As a result, the searching of more active Pt catalysts for

ammonia borane hydrolysis can be time- and effort-consuming, calling for a better understanding of the structure-performance relationship. Based on our previous study, the activity of Pt is still restricted by its poor capability to activate H_2O as schematically shown in Figure 1a, in which the indirect dissociation of H_2O has been suggested as the rate-determining step (RDS). Hence, it is reasonable to assume that the integrity of Pt with another type of active site (M), i.e., Pt-M, for the respective activation of ammonia borane and H_2O would further boost the catalytic activity of hydrogen generation.

In order to make full use of Pt-M system for the design of highly active Pt catalyst, it is highly desirable to have a fundamental understanding of the structural, chemical and electronic influences induced by the addition of another site M. Typically, the surface composition of Pt-M varies with the identity of M in terms of its atomic volume, surface energy, and heats of sublimation.[12] As a result, it has been theoretically shown that Pt atoms preferentially segregate to the interior or exterior, as well as low or high coordination sites of Pt-M particles.[13] Moreover, the presence of oxygen has also demonstrated significant influences on the structure and the resultant catalytic performance of Pt-M, which affect the stability of surface oxide species based on their aerobic and anaerobic properties.[14] Hence, although Pt-M catalysts are prepared in a reduced environment, their compositions and states might be different and how these factors evolve under atmospheric conditions is full of interest, emerging as the prerequisite for the selection of M and the integrity of Pt-M for this reaction.

On the other hand, catalyst durability is another critical criterion for the evaluation of the performance of metal catalyst that is often more important than activity for

practical application.[15] Hence, the Pt-M catalysts for ammonia borane hydrolysis should be not only active, but also durable for a long-term continuous hydrogen production. However, previous study over carbon-supported Pt catalysts found that the Pt active sites are promptly deactivated due to the agglomeration of Pt nanoparticles and the adsorption of poisonous by-products (mainly $B(OH)_4^-$) on the catalyst surface during the reaction as depicted shown in Figure 1a, so that only less than 30% of the initial catalytic activity was retained after several catalytic cycles.[7a] Unfortunately, to the best of our knowledge, few investigations have focused on protecting Pt active sites against deactivation for this reaction. Therefore, despite the easy Pt recovery by burning off the carbon support for the deactivated catalysts, it is important and timely to explore the design and preparation of a Pt-M catalyst that simultaneously achieves high activity and durability for greater ease of handling in practical application.

Herein, given the catalytic properties inherently determined by the main and secondary metal, as well as metal/support interactions, both the physical and chemical protection strategies were developed to protect Pt catalysts from deactivation in order to achieve efficient and continuous hydrogen production from ammonia borane. Physically, the mesoporous and closed-ended carbon nanotubes (CNT) were employed to support Pt particles on their external surfaces to mitigate mass transfer limitations and pore blocking by the products. Chemically, Pt was partially replaced by controlled amounts of Pd to facilitate their synergy in terms of electronic (electron transfer and repulsion) and structural (active sites engineering and steric hindrance effects) properties for this reaction. A combination of kinetic (isotopic) analyses, multiple

characterization techniques, molecular dynamics and density functional theory calculations was employed to reveal the evolution of Pt-Pd atomic structure and structure-performance relationship, and a strategy for creating Pt-PdO interfacial sites was proposed to simultaneously enhance activity and durability for hydrogen production. As a result, this study may open a new avenue for the design and preparation of highly efficient and robust metal catalysts for this reaction.

2. Experimental

2.1. *Catalyst preparation*

Mesoporous and closed-ended carbon nanotubes (CNT) were purchased from the Beijing Cnano Technology Limited (China) and were used as the catalyst support to prepare the bimetallic Pt-Pd catalysts. Typically, a certain amount of CNT was mixed with the solution of chloroplatinic acid hexahydrate ($H_2PtCl_6 \cdot 6H_2O$, Sinopharm Chemical Reagent Co., Ltd., China) and palladium chloride ($PdCl_2$, Sinopharm Chemical Reagent Co., Ltd., China). To obtain similar-sized metal catalysts, the total metal loading (Pt and Pd) was kept at 6.0 wt% for all of the catalysts. The impregnated samples were dried under stagnant air at ambient conditions and then at 80 °C for 12 h. All of the samples were reduced by a continuous flow of pure H_2 at 250 °C for 2 h, followed by cooling down to room temperature under Ar atmosphere. The reduced catalysts were passivated by exposing them to 1% O_2/Ar atmosphere for 20 min and then were stored in inert atmosphere. As a result, the as-obtained catalysts were denoted as Pt_xPd_{1-x}/CNT, where x is the Pt weight percentage.

2.2. Catalyst characterization

The particle sizes and distributions of these catalysts were measured by high-angle annular dark-field scanning transmission electron microscopy (HAADF-STEM) obtained using a Tecnai G2 F20 S-Twin instrument equipped with an energy dispersive spectrometer (EDS) analyses at 200 kV. H_2 temperature-programmed reduction (H_2-TPR) measurements were carried out using a chemisorption apparatus (Micromeritics AutoChem II 2920). The aberration-corrected high-angle annual dark-field STEM (AC-HAADF-STEM) and energy dispersive X-ray (EDS) mapping images were obtained using a JEOL ARM200F instrument with a STEM aberration (Cs) corrector operated at 200 kV. X-ray photoelectron spectroscopy (XPS) was performed using a Kratos XSAM 800 electron spectrometer (Manchester, UK) with an Al K_α X-ray (1486.6 eV) excitation source operated at 15 kV. Pt L_{III}-edge X-ray absorption fine structure (XAFS) of the catalysts was investigated at the BL14W1 beam line at the Shanghai Synchrotron Radiation Facility (SSRF) with a storage ring energy of 3.5 GeV. The X-ray beam was monochromatized by a double-crystal Si(311) monochromator. The energy was calibrated using a platinum metal foil for the Pt L_3-edge, and the WinXAS3.1 code was employed to extract and fit the data. For the X-ray absorption near edge structure (XANES) measurements, the experimental absorption coefficients as a function of energies μ(E) were obtained using background subtraction and normalization procedures.

2.3. Catalytic testing

The catalytic reaction was carried out in a three-necked flask with a Teflon-coated magnetic stirring bar that was placed in a water bath to control the reaction temperature at 30 °C. The catalyst (0.025 g) was preloaded into the flask, and the reaction was started by rapid injection of an aqueous ammonia borane solution (5 mL and 0.01 $g \cdot mL^{-1}$) via a syringe. The generated hydrogen was measured by the water displacement method. Typically, one neck of the flask was connected to a water-filled gas burette, and an electronic balance was employed to monitor the volume of discharged water, that can then be used to calculate the volume of hydrogen. Kinetic experiments for these catalysts were performed at the temperatures ranging from 25 to 40 °C under the same reaction conditions. To evaluate the catalytic durability of these catalysts, the catalytic reactions were repeated four times by adding the same amount of ammonia borane solution (5 mL and 0.01 $g \cdot mL^{-1}$) after the completion of the last cycle. After the durability test, the used catalysts were filtered from the spent solution, washed several times with deionized water and dried under vacuum at room temperature. The kinetic isotopic experiments were performed by the replacement of H_2O with D_2O as the reactant at the same reaction conditions.

2.4.Molecular dynamics calculations

The simulation of Pt-Pd nanoparticles heating was performed by molecular dynamics (MD) modeling using a large-scale atomic/molecular massively parallel simulator (LAMMPS).[16] The interaction energy between platinum and palladium atoms were described by the 12-6 Lennard-Jones potential with the parameters taken directly

from the previous study.[17] Two initial models of bimetallic Pt-Pd NPs, i.e., Janus Pt|Pd and Pd core-Pt shell, were built with simulation box size of 2.5×2.5×2.5 nm^3 to study the structural evolutions of the metal particles. For all the simulations, the velocity Verlet scheme was used to integrate the equations of motion with the time step of 1 fs, in which the periodic boundary conditions were applied in all three directions with the cut-off set to be 0.8 nm. The temperature was maintained using the Nose-Hoover thermostat with the time constant of 5 ps.[18] The steepest descent minimization was firstly conducted for the initial Pt-Pd nanoparticle structures with 8000 steps. Then, the optimized nanoparticle structures were heated in four steps with T=300 K, T=600 K, T=900 K, and T=1100 K to test their stability. The simulation time *t* for each temperature and heating from one temperature to another was set as 5 and 1 ns, respectively. The total 24 ns trajectories of the MD simulations were used to analyse the structure evolutions of the bimetallic particle with the home-built Python code based on the number of atom around each other.

2.5. Density functional theory calculations

The density functional theory (DFT) calculations were carried out by using the Vienna Ab-initio Simulation Package (VASP).[19] The projected augmented wave (PAW) pseudopotentials were chosen to describe the interaction between ion cores and valence electrons.[20] The exchange-correlation functional was calculated with generalized gradient approximation (GGA) with the Perdew-Burke-Ernzerhof (PBE) method.[21] The kinetic energy cut-off used for plane-wave expansion of electron wave functions was

450 eV for all structures.[22] A p(3 × 3) supercells with four layers was under test for the Pt and Pd slab models, which the bottom two layers of the four layers were fixed. A vacuum layer as large as 15 Å along the c direction normal to the catalyst surface was used to avoid periodic interactions. The Brillouin zone was sampled with a 3 × 3 × 1 k-point grid using Monkhorst-Pack method for all surface calculations. The energy tolerance for self-consistent iteration was set to 10^{-5} eV. The geometry optimization was converged until the residual forces on each atom were less than 0.03 eV·$Å^{-1}$. The adsorption energy of $B(OH)_4^-$ was calculated as $E_{ads} = E_{B(OH)4-/surface} - E_{B(OH)4-} - E_{surface}$, where $E_{B(OH)4-/surface}$, $E_{B(OH)4-}$ and $E_{surface}$ refer to the energy of $B(OH)_4^-$ adsorption system on metal surface, free $B(OH)_4^-$ and metal surface without adsorbates, respectively. The atomic charges and electrons transfer were investigated via the Bader analysis. On the other hand, the activation energy (E_a) is defined as $E_a=E_{TS}–E_{IS}$, in which E_{TS} and E_{IS} are the energy of the transition state (TS) and the most stable initial state (IS), respectively.

3. Results and discussion

3.1. Boosted catalytic activity and durability.

To obtain similar-sized metal catalysts, the total loadings for Pt and Pd were kept at 6.0 wt% for all of these bimetallic Pt_xPd_{1-x}/CNT catalysts. The as-prepared catalysts were characterized by HAADF-STEM with high resolution to obtain reliable metal particle size and distribution. As shown in Figure S1, all of the catalysts show similar distributions of metal particles. Based on the measurements of more than 200 random

particles, the average particle sizes for Pt/CNT, $Pt_{0.75}Pd_{0.25}$/CNT, $Pt_{0.5}Pd_{0.5}$/CNT, $Pt_{0.25}Pd_{0.75}$/CNT and Pd/CNT were determined as 2.5±0.6, 2.1±0.5, 2.2±0.6, 2.4±0.7, and 2.2±0.7 nm, respectively. Considering the metal-catalyzed ammonia borane hydrolysis as a typical structure-sensitive reaction,[7a] the similar metal particle sizes of these catalysts are beneficial for minimizing the size effect, and provide a coherent set of samples to compare the catalytic performances of different Pt/Pd ratios for ammonia borane hydrolysis based on their physical and chemical properties.

These five similar-sized catalysts were then tested for the hydrolysis of ammonia borane at the same conditions, with the results shown in Figure 1b. It is observed that the volume of generated hydrogen increases almost linearly with the reaction time at the initial stage (ammonia borane conversion lower than 45±5%), indicating a pseudo-zero reaction order with respect to ammonia borane. Therefore, it can be deduced that the reaction is not limited by external diffusion of reactants under these reaction conditions. Moreover, because the CNT used in this study is mesoporous and closed-end, the supported metal particles are deemed to be mainly located on the external surface of CNT, so that the influence of the internal diffusion limitation can also be neglected. Hence, mass transfer limitations can be minimized for these catalysts. As a result, the initial hydrogen generation rates ($r_{initial}$) values can be calculated based on the slope of the linear part of each curve, and were determined as 119.3, 88.1, 153.3, 46.3, and 27.6 $mol_{H2}\cdot g_M^{-1}\cdot h^{-1}$, respectively. It is clear that $r_{initial}$ shows a trend of decreasing with the Pd fraction, except for $Pt_{0.5}Pd_{0.5}$/CNT that delivers the highest $r_{initial}$ among all of the catalysts. This is consistent with the finding that the catalytic activity

of monometallic Pt is much higher than that of monometallic Pd, while the synergy between Pt and Pd most likely contributes to the highest catalytic activity of $Pt_{0.5}Pd_{0.5}$/CNT.

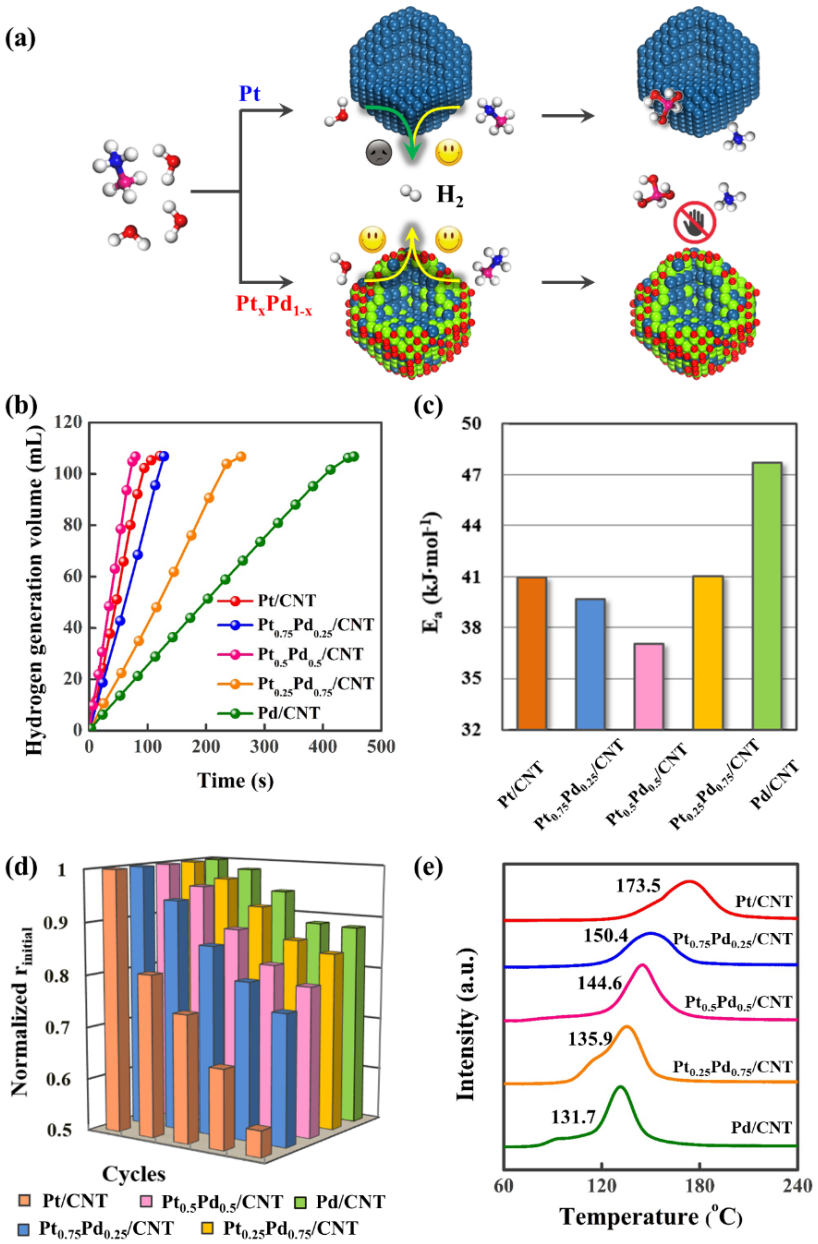

Figure 1. (a) The schematic diagram for hydrogen production activity and durability based on monometallic Pt/CNT and bimetallic Pt_xPd_{1-x}/CNT catalyst. (b) Hydrogen generation volume as a function of time, (c) activation energy (E_a), (d) relative activities over cycles, and (e) H_2-TPR profiles for Pt/CNT, $Pt_{0.75}Pd_{0.25}$/CNT, $Pt_{0.5}Pd_{0.5}$/CNT, $Pt_{0.25}Pd_{0.75}$/CNT and Pd/CNT.

For a more detailed examination, kinetic experiments were conducted for these five catalysts at different temperatures ranging from 25 to 40 °C. As shown in Figure S2, all of the catalysts still retain a linear increase of the hydrogen generation volume with reaction time at the initial stages, so that the reaction rate constant (k_H) values at different temperatures can be calculated based on low ammonia borane conversion. The Arrhenius plots of ln k_H versus 1/T presented in Figure S3 yield the activation energies (E_a) of these catalysts as 41.0, 39.6, 37.1, 41.0 and 47.7 kJ·mol^{-1} for Pt/CNT, $Pt_{0.75}Pd_{0.25}$/CNT, $Pt_{0.5}Pd_{0.5}$/CNT, $Pt_{0.25}Pd_{0.75}$/CNT and Pd/CNT, respectively. As observed in Figure 1c, $Pt_{0.5}Pd_{0.5}$/CNT with the highest catalytic activity exhibits the lowest E_a among all of these five catalysts, further highlighting that the Pt-Pd synergy within $Pt_{0.5}Pd_{0.5}$/CNT can effectively lower the energy barrier for this reaction and give the highest hydrogen generation rate.

In additional to activity, the catalytic durability was also evaluated for these five catalysts by adding the same amount of ammonia borane solution into the reaction after the completion of the last cycle, and repeating the cycle four times. As shown in Figure S4, all these catalysts exhibited a reduced hydrogen generation rate to different extents. For a clear comparison, the hydrogen generation rate in each cycle is normalized to that of the first cycle, and the results are shown in Figure 1d. It is clear that an evident increase in the catalytic durability was observed for these catalysts due to the partial replacement of Pt with Pd, with Pt/CNT, $Pt_{0.75}Pd_{0.25}$/CNT, $Pt_{0.5}Pd_{0.5}$/CNT, $Pt_{0.25}Pd_{0.75}$/CNT and Pd/CNT retaining 55%, 75%, 79%, 84% and 88% respectively, of their initial catalytic activities at the fifth cycle. Hence, although Pd exhibited a much

lower activity compared to Pt, the partial replacement of Pt with Pd gives rise to the significant synergy for simultaneously improving both the catalytic activity and durability of $Pt_{0.5}Pd_{0.5}$/CNT.

3.2. Insights into Pt-Pd atomic structure

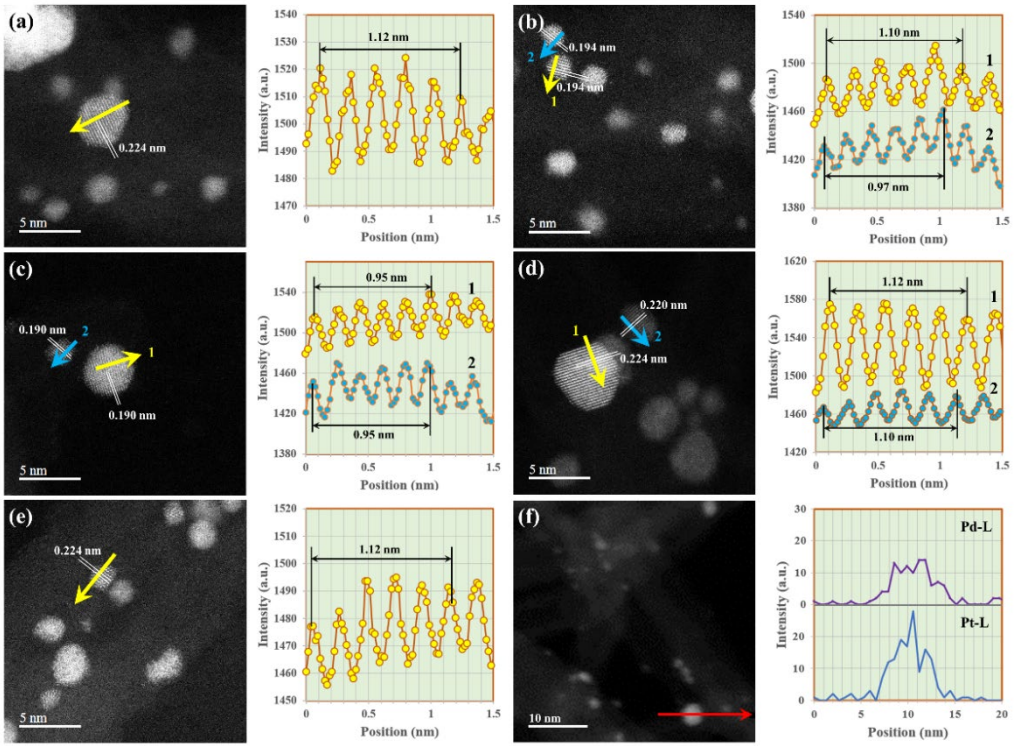

Figure 2. Typical AC-HAADF-STEM images and the corresponding line intensity profiles of (a) Pt/CNT, (b) $Pt_{0.75}Pd_{0.25}$/CNT, (c) $Pt_{0.5}Pd_{0.5}$/CNT, (d) $Pt_{0.25}Pd_{0.75}$/CNT and (e) Pd/CNT. (f) HAADF-STEM image and the corresponding EDS line-scanning image of $Pt_{0.5}Pd_{0.5}$/CNT.

H_2-TPR measurements were first conducted to probe the Pt-Pd synergy within the bimetallic Pt-Pd catalysts. Figure 1e exhibits the H_2-TPR profiles in the temperature range of 60-240 °C of the catalysts that mainly involve the peaks associated with the reduction of Pt and/or Pd species. It is clear that the monometallic Pt/CNT catalyst shows one main H_2 consumption peak at 173.5 °C, ascribed to the reduction of Pt species. With the addition of Pd, the reduction peak shifts to lower temperature and

finally reaches 131.7 °C for the monometallic Pd/CNT catalyst. Generally, the reduction temperature of the metal varies with the interaction between the metal precursor and the catalyst support. Hence, the downshift of the reduction temperature from 173.5 °C to 131.7 °C indicates a lower stability of the metal precursor, either intrinsically less stable or stabilized by the support. Based on this, it is reasonable to deduce that the Pd reduced at lower temperature can provide dissociated hydrogen for the reduction of Pt, resulting in the lower reduction temperature of bimetallic catalysts compared with the monometallic Pt/CNT catalyst.

The morphologies of these five catalysts were characterized by aberration-corrected HAADF-STEM (AC-HAADF-STEM) as shown in Figure 2, where the integrated pixel intensity profiles were derived from the lines marked by the yellow and blue arrows. It was found that these catalysts present two types of lattice fringes: 0.22-0.23 nm close to the (111) lattice spacing of the face-centered cubic (fcc) Pt (~0.226nm) and Pd (~0.221 nm), and 0.19-0.20 nm close to the (200) lattice spacing of the face-centered cubic (fcc) Pt (~0.196 nm) and Pd (~0.194 nm). Moreover, the elemental distributions of platinum and palladium within the bimetallic nanoparticles were characterized by AC-HAADF-STEM. Figure 3a displays the representative AC-HAADF-STEM image of $Pt_{0.5}Pd_{0.5}$/CNT, and the corresponding EDS-mapping results in Figure 3b-3d reveal the structure of Pt-Pd alloy with the segregation of Pd from Pt in these faceted nanoparticles. This is further validated by the EDS-mapping results in Figures S5-S7. For a more detailed examination, STEM-EDS line scan was employed to investigate the elemental distribution. It is observed from Figure 2f that the catalyst shows the

maximum Pt concentration at the center of the particle, while the Pd concentration is enriched at the edge. Based on these findings, these bimetallic catalysts are likely composed of a platinum-rich core with a palladium-rich shell. Hence, the combination of the above results suggests that the bimetallic Pt-Pd particles may undergo phase segregation of Pd to the surface forming a Pd-rich shell, and of Pt to the bulk forming a Pt-rich core.

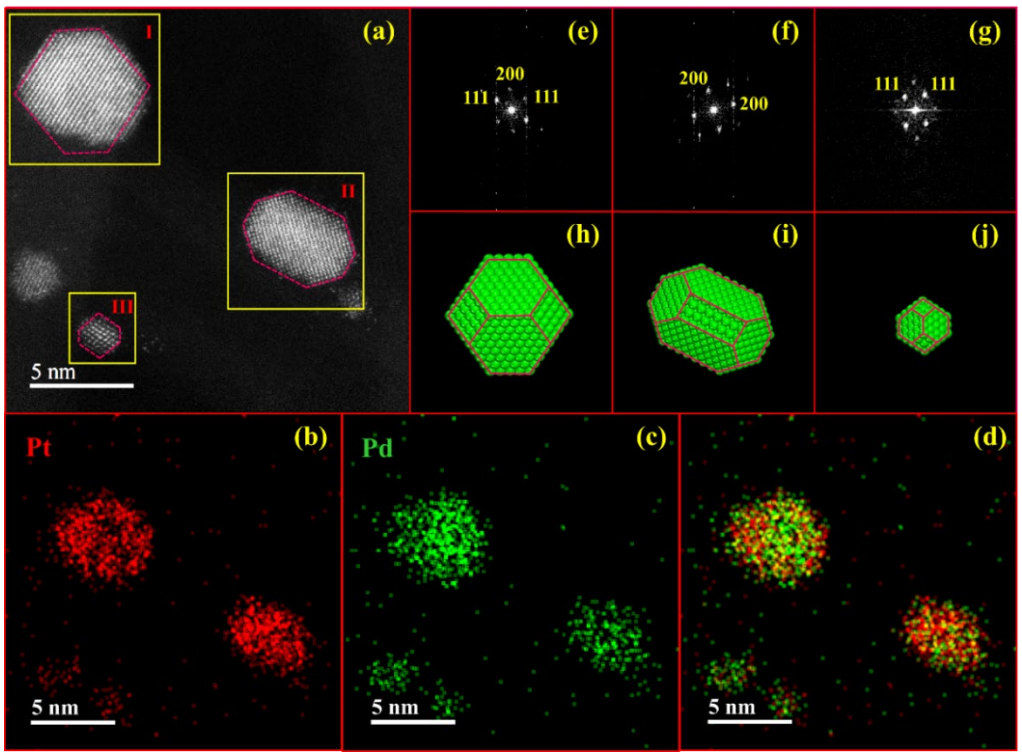

Figure 3. (a) Representative AC-HAADF-STEM image, EDS-mapping of (b) Pt, (c) Pd and (d) Pt-Pd overlay results, and (e-g) the corresponding FFT patterns of selected areas and (h-j) projections of truncated octahedron model of $Pt_{0.5}Pd_{0.5}$/CNT.

To confirm this tendency, molecular dynamics simulations and DFT calculations were employed to study the structural evolutions of the metal particles. Considering that heat treatment under hydrogen atmosphere is necessary for the precursor reduction

of these catalysts, it is possible that the atomic structures and properties of metal particles are altered during the catalyst preparation. First, the atomic structure of nanoparticles shown in Figure 3a demonstrates a typical single-crystallinity of fcc structure for which the (111) and (200) planes are directly revealed in the corresponding fast Fourier transform (FFT) as shown in Figures 3e-3g. Based on these results, the projections of the truncated octahedron model along the same direction as shown in Figures 3h-3j are quite consistent with the geometries of the three bimetallic particles shown in Figure 3a.

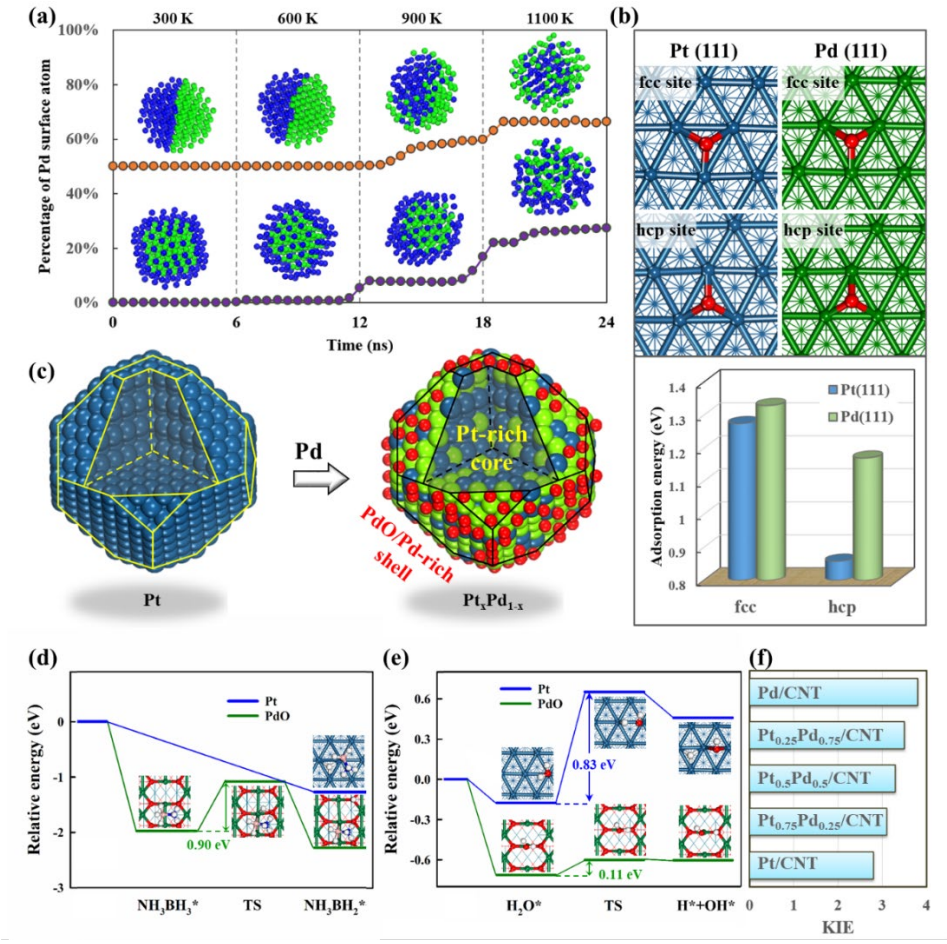

Figure 4. (a) Temperature dependence of the percentage of surface Pd atoms in the Janus Pt|Pd and Pd core-Pt shell nanoparticles. Blue and green spheres correspond to Pt and Pd atoms, respectively. (b) The diagram and corresponding absolute adsorption energy of O atoms over the fcc and hcp sites of Pt(111) and Pd(111). (c) Schematic diagram of the structure of

monometallic Pt/CNT and bimetallic Pt_xPd_{1-x}/CNT catalysts. Potential energy diagrams of (d) ammonia borane and (e) H_2O activation over Pt and PdO surfaces. (f) The kinetic isotope effect (KIE) values of Pt/CNT, $Pt_{0.75}Pd_{0.25}$/CNT, $Pt_{0.5}Pd_{0.5}$/CNT, $Pt_{0.25}Pd_{0.75}$/CNT and Pd/CNT.

As a result, the model of a truncated octahedron was selected for molecular dynamics calculations to investigate the thermal stability of the catalysts which were represented in two possible structures of bimetallic Pt-Pd nanoparticles, i.e., Janus Pt|Pd and Pd core-Pt shell, as shown in Figure 4a. It is observed that both the Janus Pt|Pd and Pd core-Pt shell nanoparticles are stable at room temperature and show significant rearrangements at temperatures higher than 600 K. It is clear from Figure 4a that the percentage of Pd surface atoms increases with the temperature for these two structures. This is consistent with the significantly different surface energies for Pd (2.00 $J \cdot m^{-2}$) and Pt (2.49 $J \cdot m^{-2}$),[21] where the Pd atoms tend to diffuse from the bulk to the surface and Pt atoms diffuse from the surface to the bulk.

Along these lines, based on the catalyst preparation procedure, the Pt-rich core and Pd-rich shell catalysts were further passivated by 1% O_2/Ar after H_2 reduction, forming a passivation layer over the particle surface to inhibit bulk oxidation. Hence, to investigate the influence of surface passivation on the atomic structure, the adsorption of O was comparably studied over Pt(111) and Pd(111) surfaces which emerge as the thermodynamically stable and most exposed facets for the fcc Pt and Pd particles, respectively. Two typical optimized adsorption sites of O atom over Pt(111) and Pd(111), i.e., fcc and hcp, are shown in Figure 4b, based on which the O adsorption energy was calculated. It is observed that for both fcc and hcp sites, the O adsorption is much

stronger on Pd(111) than that on Pt(111), particularly on the hcp site. In other words, this indicates that surface Pd atoms prefer to adsorb and bind oxygen species during the catalyst passivation, which is further verified by XPS analyses in the following sections. Based on the above analyses, it can be deduced that with the addition of Pd atoms into Pt nanoparticles, Pd atoms preferentially diffuse out onto the surface of the particles followed by partial passivation to form PdO, resulting in the bimetallic Pt-Pd catalyst with the atomic structure of a Pt-rich core and a PdO/Pd-rich shell as shown in Figure 4c.

3.3 Understanding Pt-PdO interfacial sites

Using the above information about the atomic structure of these bimetallic Pt-Pd catalyst, it is highly desirable to investigate the roles of Pt and PdO/Pd in this reaction. Considering ammonia borane and H_2O as the main reactants, their activations were comparatively studied by DFT calculations over the representative Pt(111) and PdO(101) surfaces. Figures 4d and 4e show the potential energy profiles for ammonia borane and H_2O activation, together with the structures of adsorption configurations and transition states for the Pt(111) and PdO(101) surfaces, respectively. It is clear that as shown in Figure 4d, PdO(101) exhibits a much higher activation barrier of 0.90 eV for ammonia borane activation, in comparison with the dissociative adsorption on Pt(111). In other words, Pt demonstrates a stronger capability to activate ammonia borane compared with PdO. On the other hand, the barrier for H_2O activation was determined to be 0.83 and 0.11 eV for Pt(111) and PdO(101), respectively, indicating

the high activity of H_2O dissociation over PdO. Hence, it can be predicted that the bimetallic Pt-Pd nanoparticles, involving Pt-rich core and PdO/Pd-rich shell, can work as dual catalytic site, i.e., Pt-PdO interfacial sites, for the activation of ammonia borane and H_2O, respectively.

The kinetic isotopic experiments by replacing H_2O with D_2O as the reactant were conducted to compare the abilities of these catalysts for water activation. As shown in Figure S8, all these catalysts still displayed the linear increase of hydrogen volume with reaction time, but much slower hydrogen generation rate using D_2O as the reactant. Similarly, the corresponding reaction rate constant (k_D) could be calculated based on the slope of the linear part for each curve. As a result, the ratio of the reaction rate constant using H_2O and D_2O as reactant, that is, k_H/k_D, could be calculated, which has been widely used to study kinetic isotope effects (KIE). It is clear that as shown in Figure 4f, the KIE values for these catalysts increase with the content of Pd, indicating a strong capability for water activation over the Pt-PdO interfacial sites.

To obtain the structure-performance relationship based on the interfacial sites, XPS was employed to characterize the electronic properties of these catalysts. As displayed in Figure 5a, the Pt *4f* region exhibits a doublet of Pt $4f_{5/2}$ and Pt $4f_{7/2}$. The deconvolution of the peak reveals the presence of Pt^0, Pt^{2+} and Pt^{4+}, and the corresponding percentages are summarized in Table 1. It is observed that the metallic Pt^0 remains the dominant Pt species for all of the catalysts, and its percentage first increases and then decreases with the fraction of Pd. Although metallic Pt^0 has been suggested as the main active species for the reaction, its trend is inconsistent with that of the activity, and thus could be

excluded as the main reason for the synergy between Pt-rich core and PdO/Pd-rich shell. Similarly, the Pd *3d* region in Figure 5b also displays a doublet of Pd $3d_{3/2}$ and Pd $3d_{5/2}$ that is further deconvoluted into Pd^0 and Pd^{2+}. Notably, compared with Pt, a sharp increase in the percentage of nonmetallic Pd species (Pd^{2+}), particularly for Pd/CNT, is observed due to its larger oxophilicity. This is in line with the results of the DFT calculations, and further confirms the atomic structure of the Pt-rich core and PdO/Pd-rich shell.

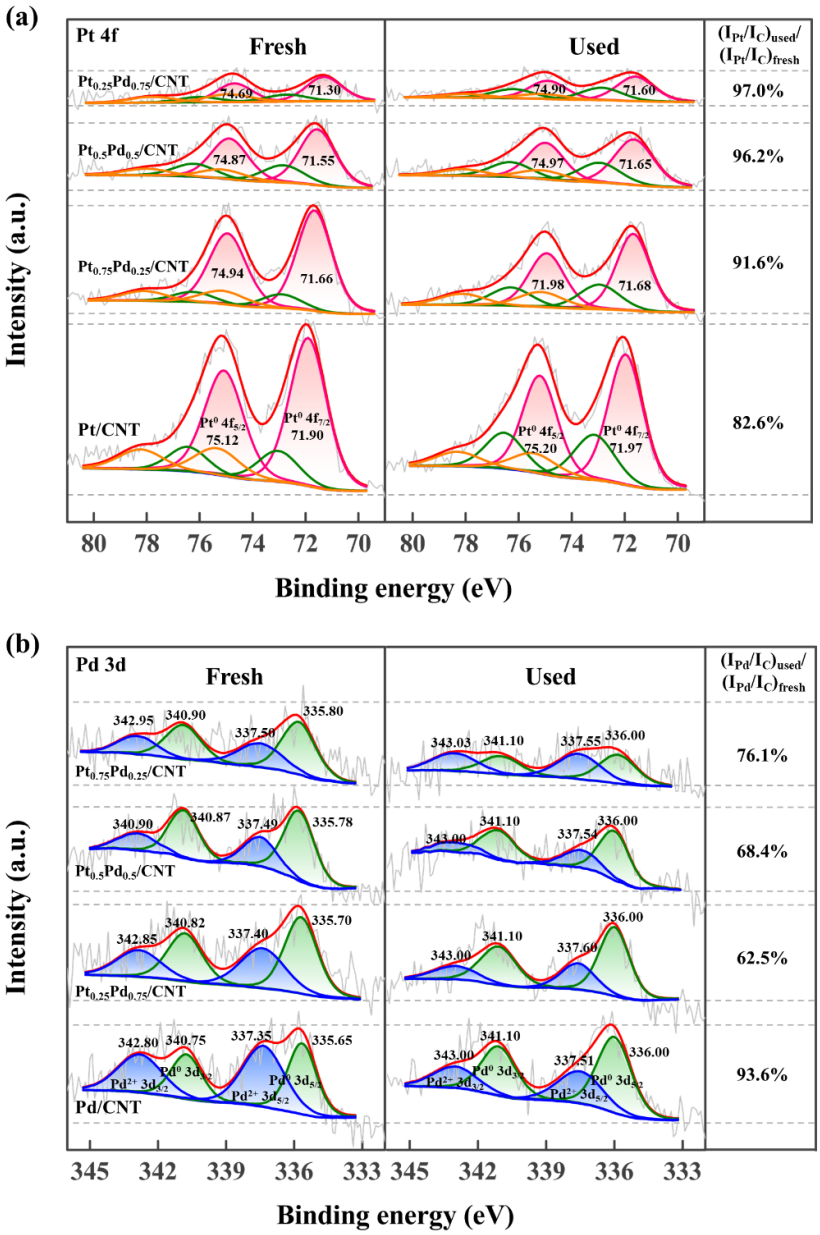

Figure 5. XPS (a) Pt *4f* and (b) Pd *3d* spectra of the fresh and used Pt/CNT, $Pt_{0.75}Pd_{0.25}$/CNT, $Pt_{0.5}Pd_{0.5}$/CNT, $Pt_{0.25}Pd_{0.75}$/CNT and Pd/CNT.

Table 1. Relative percentages of the Pt and Pd species of Pt/CNT, $Pt_{0.75}Pd_{0.25}$/CNT, $Pt_{0.5}Pd_{0.5}$/CNT, $Pt_{0.25}Pd_{0.75}$/CNT and Pd/CNT.

Catalyst	Pt percentage			Pd percentage	
	Pt^0	Pt^{2+}	Pt^{4+}	Pd^0	Pd^{2+}
Pt/CNT	69%	16%	15%	-	-
$Pt_{0.75}Pd_{0.25}$/CNT	73%	13%	14%	63%	37%
$Pt_{0.5}Pd_{0.5}$/CNT	66%	22%	12%	65%	35%
$Pt_{0.25}Pd_{0.75}$/CNT	58%	19%	23%	58%	42%
Pd/CNT	-	-	-	45%	55%

Interestingly, a downshift of the Pt binding energy from 71.90 to 71.30 eV was observed for the bimetallic Pt_xPd_{1-x}/CNT catalysts with respect to the Pt/CNT catalyst, compensated by an upshift of Pd binding energy with respect to the Pd/CNT catalyst. Because the CNT used here is highly electron-conductive and the supported metal particle sizes are similar, the observed binding energy shifts can be interpreted as the electron transfer from PdO/Pd to Pt within the bimetallic particles. To gain a more detailed understanding of the electron transfer, X-ray absorption fine structure (XAFS) technique, including X-ray absorption near edge structure (XANES) and extended X-ray absorption fine structure (EXAFS) spectroscopes, was performed to investigate the electronic structure and local coordination structure of platinum in the monometallic Pt/CNT and the bimetallic $Pt_{0.5}Pd_{0.5}$/CNT catalyst. Figure 6a displays the normalized Pt L_{III}-edge XANES profiles of these Pt catalysts and reference materials of Pt^0 (Pt foil)

and Pt^{4+} (PtO_2) standards. It is clear that the white-line (WL) peak for these two samples is nearly identical to that of the Pt foil, indicating the almost complete reduction of the Pt species. Moreover, the intensity of the WL peak follows the order of Pt foil < $Pt_{0.5}Pd_{0.5}$/CNT < Pt/CNT. Generally, the WL intensity which is an indication of the humps intensity at the Pt L_{III}-edge can reflect the electronic transition from $2p_{3/2}$ to $5d_{5/2}$ and $5d_{3/2}$ at the Pt L_{III}-edge, that can be further correlated with the electron occupancy of the Pt *5d* states. Hence, the lower WL intensity of $Pt_{0.5}Pd_{0.5}$/CNT compared with Pt/CNT indicates a higher electron filling of the Pt *5d* orbitals due to the electron transfer from PdO/Pd to Pt, thereby giving rise to the electron-rich Pt sites.

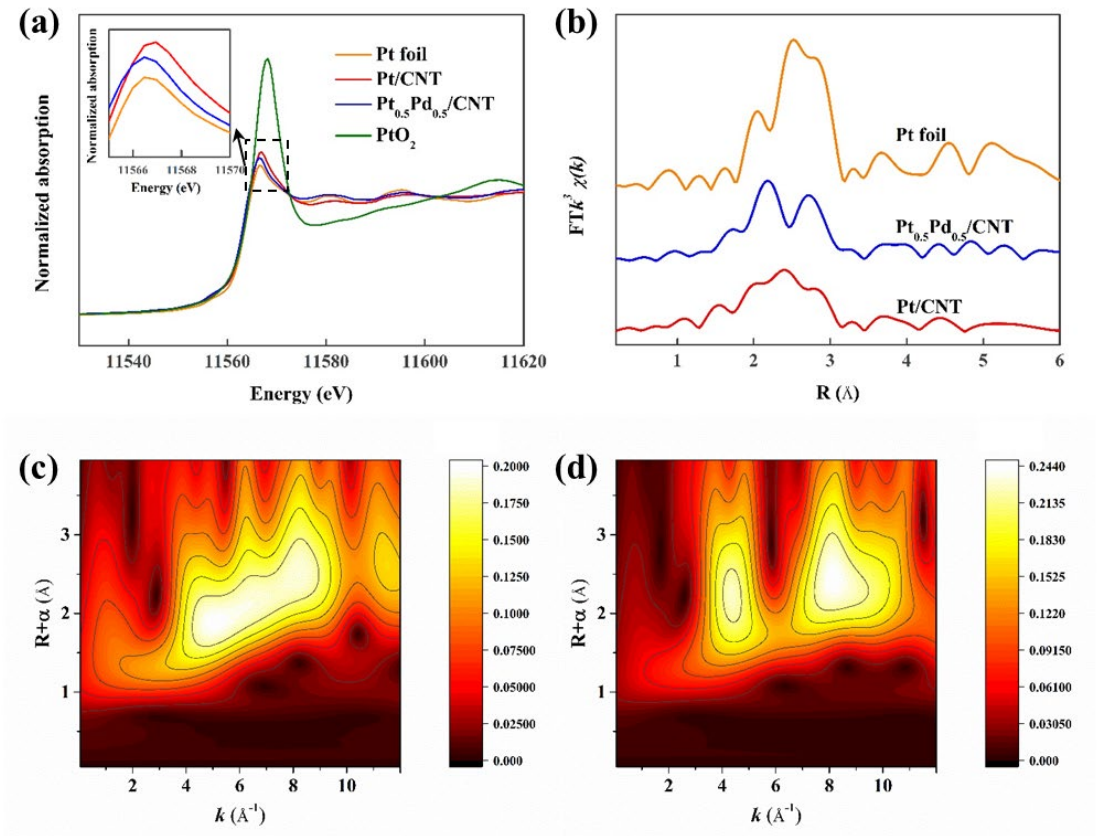

Figure 6. (a) Normalized Pt L_{III}-edge XANES spectra, (b) Fourier transformed (FT) Pt L_{III}-edge k^3-weighted EXAFS spectra of Pt/CNT and $Pt_{0.5}Pd_{0.5}$/CNT. WT-EXAFS of Pt L-edge signal of the (c) Pt/CNT (5.0 wt% Pt loading) and (d) $Pt_{0.5}Pd_{0.5}$/CNT catalyst.

Based on the previous study, a more electron-rich Pt surface with lower binding energy shows weaker bonding with the negatively charged H atom in ammonia borane.[8] Hence, this contributes to the higher activation energy barrier for the H−B bond cleavage within the ammonia borane molecule that has been identified as the prerequisite of the rate-determining step.[24] Therefore, from the point of view of electronic effects, the addition of Pd into Pt will increase the electron density of Pt and inhibit the reaction, consistent with the observed decreased catalytic activity. However, the highest catalytic activity of $Pt_{0.5}Pd_{0.5}$/CNT in terms of Pt-PdO synergy still cannot be explained by its medium binding energy, which, instead, is likely attributed to the structural effects.

Table 2. Pt L_3-edge EXAFS fitting results for the Pt/CNT (5.0 wt% Pt loading) and $Pt_{0.5}Pd_{0.5}$/CNT catalysts, and Pt foil.

Sample	shell	CN[a]	R(Å)[b]	σ^2 [c]	ΔE_0[d]	R factor[e]
Pt-foil	Pt-Pt	12*	2.76±0.01	0.0045	7.7±0.4	0.0021
Pt/CNT	Pt-C/O	1.0±0.2	2.01±0.02	0.0034		
	Pt-Cl	0.4±0.1	2.35±0.03	0.0030	7.2±1.3	0.0088
	Pt-Pt	6.8±0.4	2.74±0.01	0.0067		
$Pt_{0.5}Pd_{0.5}$/CNT	Pt-C/O	0.7±0.3	2.05±0.04	0.0034		
	Pt-Pt	5.7±0.7	2.73±0.01	0.0068	6.3±1.2	0.0086
	Pt-Pd	3.0±0.7	2.74±0.01	0.0041		

[a]*CN*: coordination numbers; [b]*R*: bond distance; [c]σ^2: Debye-Waller factors; [d]ΔE_0: the inner potential correction; [e]*R* factor: goodness of fit.

Figure 6b displays the Fourier transformed Pt L_{III}-edge k^3-weighted EXAFS spectra, and the structural parameters obtained by the aid of EXAFS fittings are listed in Table 2. It is clear that for the monometallic Pt/CNT catalyst, three strongest peaks can be observed at the distances of c.a. 2.01, 2.35 and 2.74 Å corresponding to the first shells of Pt-O/C, Pt-Cl and Pt-Pt, respectively. The lower coordination number of the Pt-Cl states indicates the low content of residual Cl species on the catalyst surface. By contrast, for the bimetallic Pt-Pd catalyst, the peak attributed to the Pt-Cl bond disappears, which could be due to the low amount of Pt on the particle surface due to its diffusion into the core. However, in light of the similar length of the Pt-Pt and Pt-Pd bond, it is difficult to visualize the difference between these two bonds by Fourier transform results in Figure 6b.

Herein, considering that the scattering neighbors with different atomic numbers are localized distinctly in k-space, the wavelet transform (WT) EXAFS, based on the correlation between R-space and k-space, was carried out to distinguish these two bonds. As displayed in Figure 6c, two major contributions were observed for the monometallic Pt/CNT catalyst, i.e., the Pt-C/O bond was located at a k value of 4-6 $Å^{-1}$ and R value of 1.9 Å, and the Pt-Pt bond was located at a k value of 7-9 $Å^{-1}$ and R value of 2.5 Å. In comparison, the bimetallic Pt-Pd catalyst in Figure 6d demonstrates another feature overlapping with the Pt-Pt bond at relatively higher k value of 9-10 $Å^{-1}$ that can be ascribed to the Pt-Pd bond. As a result, the coordination number of Pt-Pd is determined by fitting the EXAFS data as shown in Table 2. The much lower coordination number of Pt-Pd bond (3.0) with respect to Pt-Pt bond (5.7) agrees well with the phase

segregations of Pt and Pd phase within the bimetallic catalysts as schematically shown in Figure 4c. As a result, the segregation of Pd from Pt will create Pt-PdO dual catalytic site for the activation of ammonia borane and H_2O, respectively, and thus provides an explanation for the highest catalytic activity of $Pt_{0.5}Pd_{0.5}$/CNT.

The combination of the above DFT, XPS, XANES and EXAFS results suggests that PdO act as double-edged sword for the catalytic activity: on the one hand, it donates electron to Pt, and inhibits the adsorption and activation of ammonia borane, thus decreasing the catalytic activity; on the other hand, it can compensate for the poor activity of Pt to activate H_2O, and work together as dual catalytic site to increase the catalytic activity. Hence, the electronic effects in terms of electron transfer are mainly responsible for the decreased catalytic activity with the fraction of Pd, while the structural effects due to the Pt-PdO interfacial sites are mainly responsible for the highest catalytic activity of $Pt_{0.5}Pd_{0.5}$/CNT. Thus, from the point view of catalyst design, it is necessary to fabricate more Pt-PdO interfacial sites while weakening the adverse electronic effects by further optimizing the Pt/Pd ratio.

3.4 Pt-PdO synergy for catalytic durability

Interestingly, as shown in Figure 1d, the Pt-PdO interfacial sites also contribute to much higher catalytic durability of $Pt_{0.5}Pd_{0.5}$/CNT (79% of initial activity at 5^{th} cycle) compared with Pt/CNT (55% of initial activity at 5^{th} cycle). Here, because the metal particles are located on the external surface of mesoporous and closed-end CNT, the catalyst deactivation due to pore blocking by the products can be excluded. To

understand the Pt-PdO synergy for durability, the used catalysts after five cycles were filtered from the spent solution, washed by deionized water and dried under vacuum at room temperature for further characterization. The HAADF-STEM images in Figure S9 reveal the presence of a few metal particle agglomerates for the used catalysts, particularly for those with a high Pd fraction. This can be interpreted as the weaker interaction between the support and Pd with respect to Pt, as indicated by the H_2-TPR results in Figure 1e. However, the less agglomeration and stronger metal-support interaction of Pt/CNT is inconsistent with its lowest durability. In other words, this suggests that the agglomeration of metal particles is not the main reason for the differences in catalytic durability.

Similarly, the electronic properties of these used catalysts were characterized by XPS. As shown in Figures 5a and 5b, the XPS Pt *4f* and Pd *3d* spectra for these used catalysts were deconvoluted to compare with the corresponding spectra of fresh catalysts. It was found that the percentages of oxidized Pd species remain almost unchanged before and after hydrolysis reaction, which indicates less effects of H_2 generated during the hydrolysis on the reduction of PdO. Moreover, the binding energies for both Pt and Pd were observed to shift to higher values for the used catalysts. Considering that the binding energy of the metal usually decrease with its particle size, this can exclude the agglomeration of metal particles as the cause for the increased binding energy. Hence, the upshift of the metal binding energy can originate from the adsorption of B-containing by-product (mainly $B(OH)_4^-$) that can capture electrons from metal

particles.[7a,21] As a result, the B-containing by-product can strongly adsorb on metal surfaces and block them from adsorbing the reactants.

Table 3. The $(I_M/I_C)_{fresh}$, $(I_M/I_C)_{fresh}$, and $(I_M/I_C)_{used}/(I_M/I_C)_{fresh}$ based on XPS Pt *4f* and Pd *3d* spectra of Pt/CNT, $Pt_{0.75}Pd_{0.25}$/CNT, $Pt_{0.5}Pd_{0.5}$/CNT, $Pt_{0.25}Pd_{0.75}$/CNT and Pd/CNT.

Catalyst	$(I_{Pt}/I_C)_{fresh}$	$(I_{Pt}/I_C)_{fresh}$	$(I_{Pt}/I_C)_{used}/(I_{Pt}/I_C)_{fresh}$	$(I_{Pd}/I_C)_{fresh}$	$(I_{Pd}/I_C)_{used}$	$(I_{Pd}/I_C)_{used}/(I_{Pd}/I_C)_{fresh}$
Pt/CNT	3.70%	3.06%	82.7%			-
$Pt_{0.75}Pd_{0.25}$/CNT	2.21%	1.99%	90.0%	2.47%	1.84%	74.5%
$Pt_{0.5}Pd_{0.5}$/CNT	1.64%	1.58%	96.3%	2.90%	1.98%	68.3%
$Pt_{0.25}Pd_{0.75}$/CNT	0.70%	0.68%	97.1%	3.54%	2.21%	62.4%
Pd/CNT	-	-	--	4.79%	4.49%	93.7%

Hence, a semi-quantification of the B-containing by-product adsorption on the catalyst surface was conducted to compare the number of active sites before and after the durability test. Because XPS is a surface-sensitive technique and its signal intensity is proportional to the concentration of a given element per unit overlayer, it follows that the peak intensity will decrease with lower grafting density. Therefore, the intensity ratio of metal XPS signal between the used and fresh catalysts normalized to that of the C XPS signal, i.e., $(I_M/I_C)_{used}/(I_M/I_C)_{fresh}$, was used to evaluate the coverage of the B-containing by-product on the metal surface. As shown in Table 3 and Figure 5, for the monometallic Pt/CNT, the corresponding $(I_{Pt}/I_C)_{used}/(I_{Pt}/I_C)_{fresh}$ is determined to be 82.6%. With the addition of Pd, the $(I_{Pt}/I_C)_{used}/(I_{Pt}/I_C)_{fresh}$ increases from 82.6% of

Pt/CNT to 91.6%, 96.2%, and 97.0% for $Pt_{0.75}Pd_{0.25}$/CNT, $Pt_{0.5}Pd_{0.5}$/CNT and $Pt_{0.25}Pd_{0.75}$/CNT, respectively. The gradual increase of $(I_{Pt}/I_C)_{used}/(I_{Pt}/I_C)_{fresh}$ indicates that more Pt active sites are protected from the $B(OH)_4^-$ by-products poisoning with the addition of Pd. Correspondingly, the $(I_{Pd}/I_C)_{used}/(I_{Pd}/I_C)_{fresh}$ decreases from 93.6% of Pd/CNT to 62.5%, 68.4%, and 76.1% of $Pt_{0.25}Pd_{0.75}$/CNT, $Pt_{0.5}Pd_{0.5}$/CNT, and $Pt_{0.75}Pd_{0.25}$/CNT, respectively. The decline of $(I_{Pd}/I_C)_{used}/(I_{Pd}/I_C)_{fresh}$ for the bimetallic catalysts likely originates from the reduction of the surface PdO species by ammonia borane or H_2, and diffusion into the bulk, as evidenced by the decreased percentage of the Pd^{2+} species in Figure 5b. Based on the above discussion, the Pt-PdO synergy within the Pt-PdO interfacial sites will most likely significantly lower the adsorption of B-containing by-product on the metal surface that is necessary for robust hydrogen production from ammonia borane.

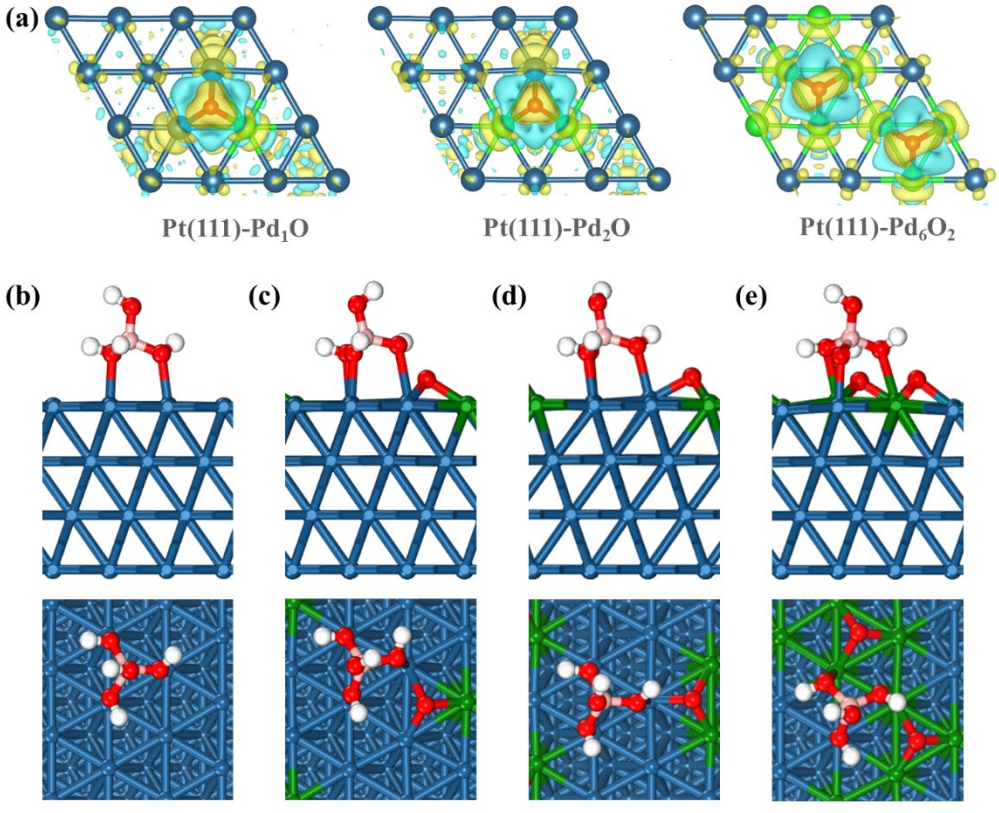

Figure 7. (a) Isosurfaces of the differential electron density for Pt(111), Pt(111)-Pd_1O, Pt(111)-Pd_2O and Pt(111)-Pd_6O_2 surfaces. Yellow and light blue isosurfaces correspond to the electron increase and depletion zones, respectively. Side view and top view of $B(OH)_4^-$ adsorbed on (b) Pt(111), (c) Pt(111)-Pd_1O, (d) Pt(111)-Pd_2O and (e) Pt(111)-Pd_6O_2.

To probe the effect of Pt-PdO synergy on catalytic durability, DFT calculations were further performed to compare the adsorption behavior of B-containing by-products, mainly $B(OH)_4^-$, on the monometallic Pt surface and the bimetallic Pt-PdO surface. Typically, three (3 × 3) slab models of the palladium-doped Pt(111) structures with different Pd atom numbers (i.e., 1, 2 and 6) were constructed as shown in Figures 7a. Based on the schematic structure shown in Figure 4c, the oxygen atoms were introduced into the slab to bind with Pd atoms that can be used to simulate the real bimetallic catalysts with different Pd contents. The as-obtained models are labelled as Pt(111)-Pd_1O, Pt(111)-Pd_2O and Pt(111)-Pd_6O_2, and the corresponding Bader charge analysis suggests the enrichment of electrons around the O atoms. Furthermore, the adsorption behaviors of $B(OH)_4^-$ on these bimetallic Pt-PdO surface are compared with that on monometallic Pt surface as shown in Figures 7b-7e. The corresponding adsorption energies of $B(OH)_4^-$ were calculated as -2.29, -1.84, -1.77 and -1.67 eV for the Pt(111), Pt(111)-Pd_1O, Pt(111)-Pd_2O and Pt(111)-Pd_6O_2 surfaces, respectively. It is clear that the addition of Pd into Pt will dramatically reduce the adsorption energy of $B(OH)_4^-$, and suppress the adsorption and poisoning of $B(OH)_4^-$ over Pt active sites, in good agreement with the trend of the catalytic durability for these catalysts. To gain a fundamental understanding of the effect of Pt-PdO synergy for durability, the

adsorption configurations of $B(OH)_4^-$ on the Pt-PdO surfaces are further compared with that on Pt. For the Pt(111) model, as shown in Figure 7b, the adsorption of $B(OH)_4^-$ leads to the formation of a Pt−O bond that is almost perpendicular to the metal surface. By increasing the surface content of PdO, as shown in Figures 7c-7e, the Pt−O bond leans toward the opposite side of PdO. Considering the negative charged oxygen in either $B(OH)_4^-$ or PdO, the change in the direction of the Pt−O bond can be interpreted as the effect of electron repulsion and steric hindrance. Thus, from the point view of either electronic or structural effects, the presence of PdO will suppress the adsorption of $B(OH)_4^-$, and protect the Pt active sites against $B(OH)_4^-$ poisoning during the reaction, thus highly promoting the catalytic durability of $Pt_{0.5}Pd_{0.5}$/CNT.

To this point, it is found that the bimetallic Pt_xPd_{1-x}CNT catalyst gives rise to not only high hydrogen generation rate but also robust catalytic durability for ammonia borane hydrolysis. As shown in Figure 1a, although the monometallic Pt displays a good capability to activate ammonia borane in terms of the B−H bond dissociation, it still needs to overcome a high activation barrier (0.83 eV) to dissociate H_2O. As a result, the NH_3BH_2* assisted dissociation of O−H bond within H_2O*, i.e., NH_3BH_2*+H_2O*→ $NH_3BH_2(OH)$*+H*, has been recognized as the rate-determining step (RDS) of the monometallic Pt catalyst for this reaction.[24] On the contrary, PdO exhibits a dramatic decline in the activation barrier (0.11 eV) for H_2O dissociation. Hence, the addition of PdO with much lower activation energy could effectively compensate for the poor activity of Pt on H_2O dissociation, and work together as Pt-PdO interfacial sites for the activations of ammonia borane and H_2O, respectively. However, the excessive addition

of Pd/PdO gives rise to much lower catalytic activity and higher activation energy in Figures 1b and 1c, which could be interpreted as the negative effect of PdO/Pd on Pt binding energy for ammonia borane activation. Based on the above analyses, like a double-edged sword, on the one hand the addition of Pd/PdO promotes H_2O activation; on the other hand, it has negative effects on Pt binding energy. Hence, the ratio of Pt to Pd/PdO is very important to achieve the trade-off between these two effects, and $Pt_{0.5}Pd_{0.5}$/CNT with the optimal ratio demonstrates the highest catalytic activity.

Moreover, the strong electron repulsion and steric hindrance effects of PdO/Pd on the adsorption of $B(OH)_4^-$ can divert these strongly adsorbed by-products away from Pt site during the reaction, giving rise to the significantly improved catalytic durability from 55% to 79% of the initial activity after 5 cycles. Based on previous studies over bimetallic Pt-Pd catalysts, it was found that the composition (Pt and Pd ratios), structure (hierarchical pores), morphology (cube and sphere) as well as facet orientations ((100) and (111) facets) have significant influences on the catalytic performance for this reaction.[25] Hence, future attempts will be made to optimize the Pt-Pd catalyst preparation procedures, including metal precursors, adding sequence, reducing method, and protective agent, thus combining the Pt-PdO interfacial sites in this study with the merits of the above factors to further improve hydrogen generation.

4. Conclusions

In summary, we have demonstrated a strategy to promote both catalytic activity and durability of the Pt catalyst for hydrogen production from ammonia borane by the

utilization of CNT as support and Pd as the structural and electronic promoter. This promotion effect has been explored by a combination of kinetic (isotopic) analyses, multiple characterization, molecular dynamics and density functional theory calculations. Physically, the Pt particles supported on the external surface of mesoporous and closed-end CNT can mitigate mass transfer limitations and pore blocking by the products generated during the reaction. Chemically, it is found that the bimetallic Pt-Pd catalysts undergo the evolution of Pd segregation to the outer surface of Pt nanoparticles followed by partial oxidation, and mainly present in a unique atomic structure of a Pt-rich core and a PdO/Pd-rich shell structure, creating Pt-PdO interfacial sites for ammonia borane and H_2O activation, respectively. The strong capability of PdO to activate H_2O compensates for its adverse effects on the Pt electronic properties for ammonia borane dissociation, contributing to the highest catalytic activity for $Pt_{0.5}Pd_{0.5}$/CNT. Moreover, due to the electron repulsion and steric hindrance effects, the PdO sites on the catalyst surface can strongly suppress the adsorption of $B(OH)_4^-$ byproducts, thus protecting the Pt active sites from poisoning and endowing them with enhanced catalytic durability for long-term hydrogen production. As a result, $Pt_{0.5}Pd_{0.5}$/CNT with the optimal Pt/Pd ratio appears to be the most promising catalyst at the apex of volcano curve, in which significant improvements in both activity and durability are achieved. The insights gained here could shed new light on the design and fabrication of efficient and durable catalysts for ammonia borane hydrolysis.

Acknowledgments

This work was financially supported by the Natural Science Foundation of China (21922803 and 21776077), the China Postdoctoral Science Foundation (BX20190116), the Program for Professor of Special Appointment (Eastern Scholar) at Shanghai Institutions of Higher Learning, the State Key Laboratory of Organic-Inorganic Composites (oic-201801007), 111 Project of the Ministry of Education of China (B08021) and the Open Project of State Key Laboratory of Chemical Engineering (SKLChe-15C03). The authors thank beamline BL14W1 (Shanghai Synchrotron Radiation Facility) for the beam time and assistant in the experiments.

Reference

(1) (a) Zhang, L.; Zhou, M.; Wang, A.; Zhang, T. Selective Hydrogenation Over Supported Metal Catalysts: from Nanoparticles to Single Atoms. *Chem. Rev.* **2019**, 120, 683−733. (b) Matsubu, J. C.; Zhang, S.; DeRita, L.; Marinkovic, N. S.; Chen, J. G.; Graham, G. W.; Pan, X.; Christopher, P. Adsorbate-Mediated Strong Metal–Support Interactions in Oxide-Supported Rh Catalysts. *Nat. Chem.* **2017**, 9, 120−127. (c) van Deelen, T. W.; Nijhuis, J. J.; Krans, N. A.; Zecevic, J.; de Jong, K. P. Preparation of Cobalt Nanocrystals Supported on Metal Oxides to Study Particle Growth in Fischer-Tropsch Catalysts. *ACS Catal.* **2018**, 8, 10581−10589. (d) Xu, J.; Zhang, C.; Liu, H.; Sun, J.; Xie, R.; Qiu, Y.; Lu, F.; Liu, Y.; Zhuo, L.; Liu, X.; Luo, J. Amorphous MoO_X-Stabilized Single Platinum Atoms with Ultrahigh Mass Activity for Acidic Hydrogen Evolution. *Nano Energy* **2020**, 70, 104529.

(2) (a) Kattel, S.; Ramirez, P. J.; Chen, J. G.; Rodriguez, J. A.; Liu, P. Active Sites for CO_2 Hydrogenation to Methanol on Cu/ZnO Catalysts. *Science* **2017**, 355, 1296−1299. (b) Porosoff, M. D.; Yan, B.; Chen, J. G. Catalytic Reduction of CO_2 by H_2 for Synthesis of CO, Methanol and Hydrocarbons: Challenges and Opportunities. *Energ. Environ. Sci.* **2016**, 9, 62−73. (c) Han, L.; Song, S.; Liu, M.; Yao, S.; Liang, Z.; Cheng, H.; Ren, Z.; Liu, W.; Lin, R.; Qi, G.; Liu, X. Stable and Efficient Single-Atom Zn Catalyst for CO_2 Reduction to CH_4. *J. Am. Chem. Soc.* **2020**, 142, 12563−12567.

(3) (a) Christopher, P.; Xin, H.; Linic, S. Visible-Light-Enhanced Catalytic Oxidation Reactions on Plasmonic Silver Nanostructures. *Nat. Chem.* **2011**, 3, 467−472. (b) Bligaard, T.; Bullock, R. M.; Campbell, C. T.; Chen, J. G.; Gates, B. C.; Gorte, R. J.; Jones, C. W.; Jones, W. D.; Kitchin, J. R.; Scott, S. L. Toward Benchmarking in Catalysis Science: Best Practices, Challenges, and Opportunities. *ACS Catal.* **2016**, 6, 2590−2602. (c) Calle-Vallejo, F.; Loffreda, D.; Koper, M. T.; Sautet, P. Introducing Structural Sensitivity into Adsorption–Energy Scaling Relations by Means of Coordination Numbers. *Nat. Chem.* **2015**, 7, 403−410. (d) Cargnello, M.; Jaen, J. D.; Garrido, J. H.; Bakhmutsky, K.; Montini, T.; Gamez, J. C.; Gorte, R. J.; Fornasiero, P. Exceptional Activity for Methane Combustion over Modular Pd@ CeO_2 Subunits on Functionalized Al_2O_3. *Science* **2012**, 337, 713−717.

(4) (a) Zheng, Y.; Jiao, Y.; Zhu, Y.; Li, L. H.; Han, Y.; Chen, Y.; Du, A.; Jaroniec, M.; Qiao, S. Z. Hydrogen Evolution by A Metal-Free Electrocatalyst. *Nat. Commun.*

2014, 5, 1−8. (b) Suh, M. P.; Park, H. J.; Prasad, T. K.; Lim, D. W. Hydrogen Storage in Metal–Organic Frameworks. *Chem. Rev.* **2012**, 112, 782−835.

(5) (a) Demirci, U. B. Ammonia Borane, A Material with Exceptional Properties for Chemical Hydrogen Storage. Int. J. Hydrogen Energ. **2017**, 42, 9978−10013. (b) Sanyal, U.; Demirci, U. B.; Jagirdar, B. R.; Miele, P. Hydrolysis of Ammonia Borane as A Hydrogen Source: Fundamental Issues and Potential Solutions towards Implementation. *ChemSusChem* **2011**, 4, 1731-1739. (c) Demirci, U. B.; Miele, P. Hydrolysis of Solid Ammonia Borane. *J. Power Sources* **2010**, 195, 4030−4035.

(6) (a) Zhan, W. W.; Zhu, Q. L.; Xu, Q. Dehydrogenation of Ammonia Borane by Metal Nanoparticle Catalysts. *ACS Catal.* **2016**, 6, 6892−6905. (b) Jiang, H. L.; Xu, Q. Catalytic Hydrolysis of Ammonia Borane for Chemical Hydrogen Storage. *Catal. Today* **2011**, 170, 56−63. (c) Li, Z.; He, T.; Matsumura, D.; Miao, S.; Wu, A.; Liu, L.; Wu, G.; Chen, P. Atomically Dispersed Pt on the Surface of Ni Particles: Synthesis and Catalytic Function in Hydrogen Generation from Aqueous Ammonia–Borane. *ACS Catal.* **2017**, 7, 6762−6769.

(7) (a) Chen, W.; Ji, J.; Feng, X.; Duan, X.; Qian, G.; Li, P.; Zhou, X.; Chen, D.; Yuan, W. Mechanistic Insight into Size-Dependent Activity and Durability in Pt/CNT Catalyzed Hydrolytic Dehydrogenation of Ammonia Borane. *J. Am. Chem. Soc.* **2014**, 136, 16736−16739. (b) Zhang, J.; Chen, C.; Chen, S.,; Hu, Q.; Gao, Z.; Li, Y.; Qin, Y. Highly Dispersed Pt Nanoparticles Supported on Carbon Nanotubes Produced by Atomic Layer Deposition for Hydrogen Generation from Hydrolysis of Ammonia Borane. *Catal. Sci. Tech.* **2017**, 7, 322−329.

(8) Chen, W.; Ji, J.; Duan, X.; Qian, G.; Li, P.; Zhou, X.; Chen, D.; Yuan, W. Unique Reactivity in Pt/CNT Catalyzed Hydrolytic Dehydrogenation of Ammonia Borane. *Chem. Commun.* **2014**, 50, 2142−2144.

(9) (a) Wang, S.; Zhang, D.; Ma, Y.; Zhang, H.; Gao, J.; Nie, Y.; Sun, X. Aqueous Solution Synthesis of Pt-M (M= Fe, Co, Ni) Bimetallic Nanoparticles and Their Catalysis for the Hydrolytic Dehydrogenation of Ammonia Borane. *ACS Appl. Mater. Inter.* **2014**, 6, 12429−12435. (b) Karaca, T.; Sevim, M.; Metin, O. Facile Synthesis of Monodisperse Copper–Platinum Alloy Nanoparticles and Their Superb Catalysis in the Hydrolytic Dehydrogenation of Ammonia Borane and Hydrazine Borane. *ChemCatChem* **2017**, 9, 4185−4190.

(10) (a) Chen, W.; Wang, Z.; Duan, X.; Qian, G.; Chen, D.; Zhou, X. Structural and Kinetic Insights into Pt/CNT Catalysts during Hydrogen Generation from Ammonia Borane. *Chem. Eng. Sci.* **2018**, 192, 1242−1251. (b) Chen, Y.; Yang, X.; Kitta, M.; Xu, Q. Monodispersed Pt Nanoparticles on Reduced Graphene Oxide by A Non-Noble Metal Sacrificial Approach for Hydrolytic Dehydrogenation of Ammonia Borane. *Nano Res.* **2017**, 10, 3811−3816.

(11) Chen, W.; Fu, W.; Chen, B.; Peng, C.; Qian, G.; Chen, D.; Duan, X.; Zhou, X. Polymer Decoration of Carbon Support to Boost Pt-Catalyzed Hydrogen Generation Activity and Durability. *J. Catal.* **2020**, 385, 289−299.

(12) (a) Xu, Y.; Ruban, A. V.; Mavrikakis, M. Adsorption and Dissociation of O_2 on Pt−Co and Pt−Fe Aloys. *J. Am. Chem. Soc.* **2004**, 126, 4717−4725. (b) Lubarda, V.

A. On the Effective Lattice Parameter of Binary Alloys. *Mech. Mater.* **2003**, 35, 53−68.

(13) (a) Chepkasov, I. V.; Visotin, M. A.; Kovaleva, E. A.; Manakhov, A. M.; Baidyshev, V. S.; Popov, Z. I. Stability and Electronic Properties of PtPd Nanoparticles via MD and DFT calculations. *J. Phys. Chem. C* **2018**, 122, 18070−18076. (b) Wang, G.; Van Hove, M. A.; Ross, P. N.; Baskes, M. I. Quantitative Prediction of Surface Segregation in Bimetallic Pt–M Alloy Nanoparticles (M=Ni, Re, Mo). Prog. *Surf. Sci.* **2005**, 79, 28−45.

(14) (a) Gu, Z.; Balbuena, P. B. Atomic Oxygen Absorption into Pt-based Alloy Subsurfaces. *J. Phys. Chem. C* **2008**, 112, 5057−5065. (b) Ramirez-Caballero, G. E.; Balbuena, P. B. Surface Segregation of Core Atoms in Core–Shell Structures. *Chem. Phys. Lett.* **2008**, 456, 64-67.

(15) (a) Yano, H.; Watanabe, M.; Iiyama, A.; Uchida, H. Particle-Size Effect of Pt Cathode Catalysts on Durability in Fuel Cells. *Nano Energy* **2016**, 29, 323−333. (b) Chen, T. W.; Huang, W. F.; Kang, J. X.; Zhang, D. F.; Guo, L. Cycling Potential Engineering Surface Configuration of Sandwich Au@Ni@PtNiAu for Superior Catalytic Durability. *Nano Energy* **2018**, 52, 22−28.

(16) Plimpton, S. Fast Parallel Algorithms for Short-Range Molecular Dynamics. *J. Comp. Physiol.* **1995**, 117, 1−19.

(17) Heinz, H.; Vaia, R. A.; Farmer, B. L.; Naik, R. R. Accurate Simulation of Surfaces and Interfaces of Face-Centered Cubic Metals Using 12−6 and 9−6 Lennard-Jones Potentials. *J. Phys. Chem. C* **2008**, 112, 17281−17290.

(18) (a) Nose, S. A Molecular Dynamics Method for Simulations in the Canonical Ensemble. Mol. Phys. 1984, 52, 255−268. (b) Nose, S. A Unified Formulation of the Constant Temperature Molecular Dynamics Methods. J. Phys. Chem. 1984, 81, 511−519. (c) Hoover, W. G. *Time Reversibility, Computer Simulation, and Chaos;* World Scientific: Singapore, 1999.

(19) (a) Kresse, G.; Hafner, J. Ab Initio Molecular Dynamics for Liquid Metals. *Phys. Rev. B* **1993**, 47, 558−561. (b) Kresse, G.; Hafner, J. Ab Initio Molecular-Dynamics Simulation of the Liquid-Metal-Amorphous-Semiconductor Transition in Germanium. *Phys. Rev. B* **1994**, 49, 14251−14269. (c) Kresse, G.; Furthmuller, J. Efficiency of Ab-Initio Total Energy Calculations for Metals and Semiconductors Using a Plane-Wave Basis Set. *Comp. Mater. Sci.* **1996**, 6, 15-50. (d) Kresse, G.; Furthmuller, J. Efficient Iterative Schemes for Ab Initio Total-Energy Calculations Using a Plane-Wave Basis Set. *Phys. Rev. B* **1996**, 54, 11169−11186.

(20) Blochl, P. E. Projector Augmented-Wave Method. *Phys. Rev. B* **1994**, 50, 17953−17979.

(21) Perdew, J. P.; Burke K.; Ernzerhof M. Generalized Gradient Approximation Made Simple. *Phys. Rev. Lett.* **1996**, 77, 3865−3868.

(22) Monkhorst, H. J.; Pack, J. D. Special Points for Brillouin-Zone Integrations. *Phys. Rev. B* **1976**, 13, 5188−5192.

(23) Tyson, W. R.; Miller, W. A. Surface Free Energies of Solid Metals: Estimation From Liquid Surface Tension Measurements. *Surf. Sci.* **1977**, 62, 267−276.

(24) Chen, W.; Li, D.; Wang, Z.; Qian, G.; Sui, Z.; Duan, X.; Zhou, X.; Yeboah, I.; Chen, D. Reaction Mechanism and Kinetics for Hydrolytic Dehydrogenation of Ammonia Borane on A Pt/CNT Catalyst. *AIChE J.* **2017**, 63, 60−65.

(25) (a) Yao, K.; Zhao, C.; Wang, N.; Li, T.; Lu, W.; Wang, J. An Aqueous Synthesis of Porous PtPd Nanoparticles with Reversed Bimetallic Structures for Highly Efficient Hydrogen Generation from Ammonia Borane Hydrolysis. *Nanoscale* **2020**, 12, 638−647. (b) Amali, A. J.; Aranishi, K.; Uchida, T.; Xu, Q. PdPt Nanocubes: A High-Performance Catalyst for Hydrolytic Dehydrogenation of Ammonia Borane. *Part. Part. Syst. Char.* **2013**, 30, 888−892. (c) Zhang, Z.; Jiang, Y.; Chi, M.; Yang, Z.; Wang, C.; Lu, X. Electrospun Polyacrylonitrile Nanofibers Supported Alloyed Pd-Pt Nanoparticles as Recyclable Catalysts for Hydrogen Generation from the Hydrolysis of Ammonia Borane. *RSC Adv.* **2015**, 5, 94456−94461.

Table of Contents